



Comparison of laser-MIG hybrid and autogenous laser welding of M250 maraging steel thick sections—understanding the role of filler wire addition

L. Subashini^{1,2} · K. V. Phani Prabhakar¹ · Swati Ghosh² · G. Padmanabham¹

Received: 19 July 2019 / Accepted: 17 February 2020 / Published online: 3 March 2020
© Springer-Verlag London Ltd., part of Springer Nature 2020

Abstract

The present work is directed towards understanding the role of filler addition in laser-MIG hybrid welding (LHW) process as compared with that in autogenous laser welding (ALW) process during welding of 10-mm-thick maraging steel plates. Addition of filler wire is beneficial in improving the edge bridging between the parts to be welded and also in improving the fusion zone microstructure. Single-pass LHW of the 10-mm-thick maraging steel plates was performed using a combination of 3.5-kW CO₂ laser and synergic pulse MIG welding power source at a welding speed of 1 m/min. MIG filler wire with reduced solutes such as Mo and Ti contents was used for the LHW process. Simultaneously, double-sided single-pass ALW of similar plates was performed. The role of filler wire addition on the microstructure and mechanical properties of the LHW fusion zone (FZ) was studied and compared with that of ALW FZ. The usage of filler wire resulted in less solutes in the LHW FZ after welding, and hence, the volume fraction of “reverted austenite (RA)” formed during aging was minimized when compared with ALW FZ. During transverse weld tensile testing, the ALW welds yielded higher tensile properties when compared with the LHW weld due to their fine grain structure and high number density of precipitates. Whereas the K_{Ic} fracture toughness of the ALW FZ was low with the K_{Ic} value of 49.5 MPa√m due to the presence of the high amount of RA as compared with LHW which exhibited the K_{Ic} value of 77.5 MPa√m. The study vividly brings out the advantages of LHW process in improving the microstructure of the fusion zone due to the addition of filler wire.

Keywords M250 · Maraging · Welding · Laser · Hybrid · Filler · Fusion

1 Introduction

Maraging steels are very low-carbon, Fe-Ni alloy systems with varying percentage of Co, Mo, and Ti designed for applications requiring a combination of high strength with good fracture toughness. These superior properties are obtained due to the combination of two solid-state reactions “MAR + AGING,” meaning martensite formation and aging [1]. The microstructure of these steels in thermally aged condition has fine intermetallic precipitates, viz., Ni₃Ti, Ni₃Mo, and Fe₂Mo,

distributed uniformly throughout a soft and tough Fe-Ni lath martensite matrix [2]. The M250 grade maraging steels that are used in applications such as rocket motor casings require thick sections in welded condition. These steels are welded in solution annealed condition followed by a simple post-weld aging treatment at ~480 °C [3].

Welding of M250 grade maraging steel thick sections is commonly done by multiple passes of gas tungsten arc welding (GTAW) process employing a wide V-groove joint preparation. In most cases, joint efficiencies up to 90–95% could be achieved with respect to tensile strength [4–6]. The main concern in maraging steel welds is deterioration of fusion zone toughness due to the formation of white pools of “reverted austenite” (RA) phase. RA appears in the microstructure of the weld fusion zone at interdendritic regions after post-weld aging treatment. These are regions where solute elements Ni, Mo, and Ti had segregated during weld metal solidification, which reduce austenite start temperature (A_s)

✉ G. Padmanabham
director@arci.res.in; gp@arci.res.in

¹ Centre for Laser Processing of Materials, International Advanced Research Centre for Powder Metallurgy and New Materials (ARCI), Balapur PO, Hyderabad 500005, India

² School of Engineering Sciences and Technology, University of Hyderabad, Hyderabad 500046, India

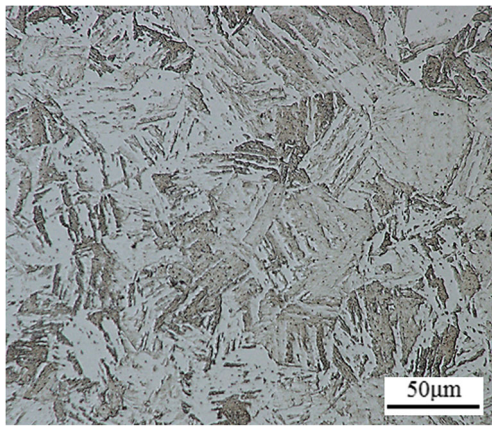


Fig. 1 Microstructure of the as-received base metal

below normal aging temperature and form soft RA pools devoid of intermetallic precipitates. During testing, precipitate-free soft RA pools cracked preferentially because slip takes place in it at stresses which are too low to produce slip in the hard martensite matrix [6].

Filler material composition noticeably influences the mechanical properties of maraging steel welds [7]. During GTAW and gas metal arc welding (GMAW), only when both the Ti and Mo contents were reduced in the filler metal, RA formation was prevented and toughness of the weld fusion zone improved [6, 8]. Post-weld heat treatments such as homogenization treatment and solutionizing treatment before aging reduced the reverted austenite at the interdendritic boundaries and resulted in improved mechanical properties [5, 7]. The high energy density fusion processes, viz. laser beam welding [9–12] and electron beam welding [13], were potential alternate methods for fabrication of aerospace components like airframe sections, rocket motor casings with superior weld quality, and negligible distortion [14, 15]. Electron beam and laser welding were used satisfactorily to weld thin sheets to moderately thick plates of maraging steel, but as the thickness of the plate increases, it becomes difficult to achieve a very low edge gap and a precise joint fit-up. However, autogenous laser butt welds of M250 maraging steel exhibited reduced mechanical properties which were attributed to the combination of misalignment of joint with the beam, weld geometry, and RA in the weld metal [12]. Recent study on single-pass keyhole plasma arc welding (PAW) of 8-mm-thick M250 plates concluded that the PAW welds exhibited improved mechanical and metallurgical properties in comparison with multi-pass GTAW. PAW welds showed about 3 to

Table 1 Base metal and filler wire composition (wt%)

Elements	C	Ni	Co	Mo	Ti	Al	Fe
M250 steel base metal	0.01	18	7.75	4.9	0.40	0.10	Bal
W2 filler wire	0.0075	18	11.75	2.4	0.14	0.15	Bal

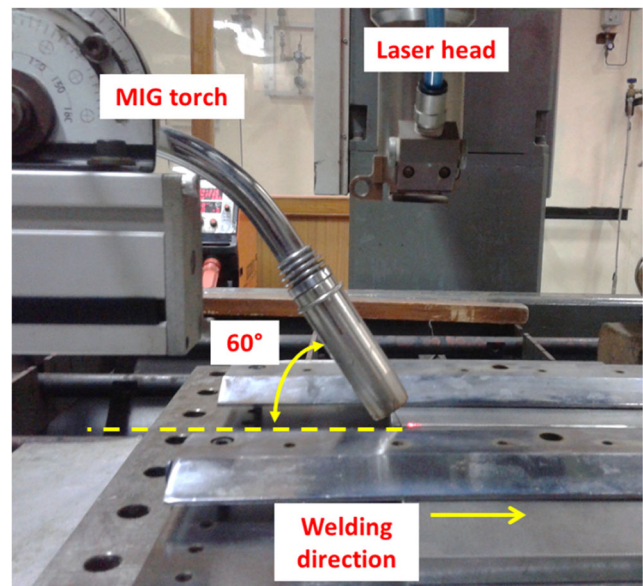


Fig. 2 Arrangement of CO₂ laser-MIG welding process setup

4% improvement in strength values and K_{Ic} values compared with GTAW welds [16]. By single-pass welding, the heat input experienced by the material is reduced which may possibly result in reduced amount of deleterious phases formed in the welds. Welding of thick plates in a single pass is advantageous from both the process and metallurgical points of view. In this context, laser hybrid welding which is the combination of arc and laser beam welding produces a single high intensity energy source enabling full penetration welds of thicker sections in a single pass at a comparatively low heat input, eliminating the need for additional passes [17]. For example, a laser hybrid welding system combining a 3.5-kW CO₂ laser and synergic pulse MIG welding power source was successfully used to weld 12-mm-thick steel plates in a single pass [18]. LHW is being used in shipbuilding, pipeline, automotive industries, and the laser hybrid weldability of various alloy systems including stainless steels, advanced high strength steels, and Al, Mg, and Ti alloys has been investigated [19–23]. Single-pass laser-MIG hybrid welding of 10-mm-thick plates of M250 maraging steels reported advantages in terms of process parameters such as high welding speed, reduced filler wire consumption, and reduced heat input together with minimization of the size and amount of reverted austenite in the fusion zone [24].

In the present study, single-pass laser-MIG hybrid welding (LHW) of 10-mm-thick maraging steel plates was performed using a combination of 3.5-kW CO₂ laser and synergic pulse MIG welding power source. MIG filler wire with reduced solutes such as Mo and Ti contents was used for the LHW process. Simultaneously, double-sided single-pass autogenous laser welding (ALW) of similar plates was performed. The role of filler wire addition on the microstructure and mechanical properties of the LHW fusion zone was studied and

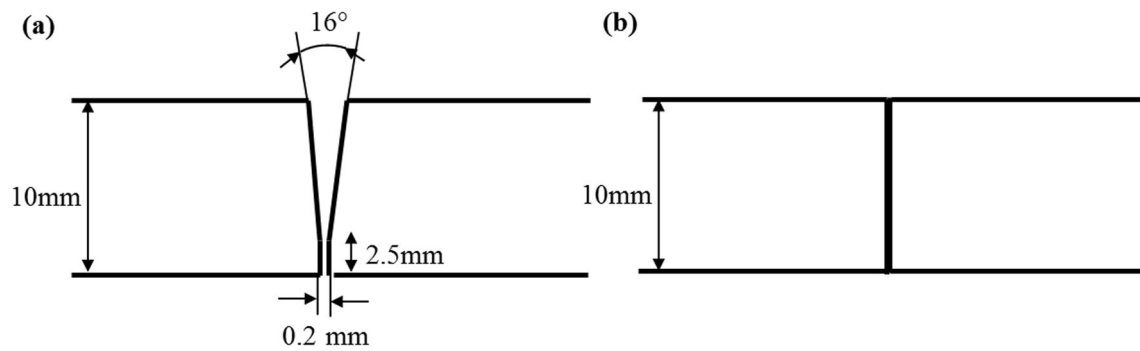


Fig. 3 Schematic of the joint designs for **a** LHW and **b** ALW

compared with that of the ALW fusion zone. The major objectives of the study are to understand the role of filler wire addition in the LHW process in comparison with that in the ALW process vis-à-vis fusion zone chemistry, amount of reverted austenite, tensile, and fracture toughness of the welds.

2 Materials and methods

M250 grade maraging steel plates of 10 mm thickness received in solution annealed condition were used for the study. The as-received base metal microstructure is shown in Fig. 1. It consisted of a single-phase structure of lath martensite. Filler wire M250 W2 type having a diameter of 1.2 mm was used for laser-MIG hybrid welding. It had high cobalt and low molybdenum and titanium content as compared with the base material. The filler composition was designed to minimize segregation of solute elements during weld metal solidification. The chemical compositions of base material and filler wire are given in Table 1.

The laser hybrid welding system comprised the Rofin DC035 slab CO₂ laser integrated with KEMPPI PROMIG 530 (Synergic) welding system, as shown in Fig. 2. The laser beam of a wavelength of 10.6 μm in Gaussian beam mode ($K > 0.9$) was used. A 300-mm focal length mirror was used to get a laser beam spot size of 180 μm. The MIG welding system was integrated with laser in such a way that the arc

and laser can operate together. The distance between sources was maintained between 2 and 3 mm, with laser leading the MIG torch. The plates were prepared with a Y-groove edge configuration, 16° included angle, and a root face height of 2.5 mm as shown in Fig. 3 a. A root gap of 0.2 mm was maintained between the plates during welding. The shielding gas mixture of 80% He + 20% Ar was passed through the MIG welding torch. Laser-MIG hybrid welding was performed with a laser power of 3.5 kW and MIG wire feed rate of 12 m/min at a welding speed of 1 m/min. Autogenous laser welding was performed on plates with straight I joint preparation as shown in Fig. 3 b. Laser power of 3.5 kW at 1 m/min welding speed resulted in 6.5-mm weld penetration. Hence, double-sided single-pass laser welding was done. One hundred percent He shielding was used for the experiments. The optimized process parameters involved in both the welding processes are tabulated and compared in Table 2. After welding, dye penetrant testing was conducted to identify surface defects, followed by radiography inspection. After this, the weld pads were subjected to post-weld aging treatment of 480 °C for 3 ½ h.

Macro- and micrography studies were conducted in the as-welded and post-weld aged conditions in the LHW and ALW welds. Transverse weld cross sections were mounted and polished following standard metallographic procedures. Macroetching was done according to ASTM E340 by immersing the specimen in a solution of 50 mL HCl, 25 mL HNO₃,

Table 2 LHW and ALW welding process parameters

Process	LHW	ALW
Nature of joint	Single pass	Double-sided single pass
Laser power (kW)	3.5	3.5
Focal plane position from surface (mm)	7.5	On surface
Wire feed rate (m/min)	12	-
Current (A)	302	-
Voltage (V)	39.4	-
Welding speed (m/min)	1	1
Shielding gas	80% He–20% Ar	100% He
Total heat input (J/mm)	817	210 per pass

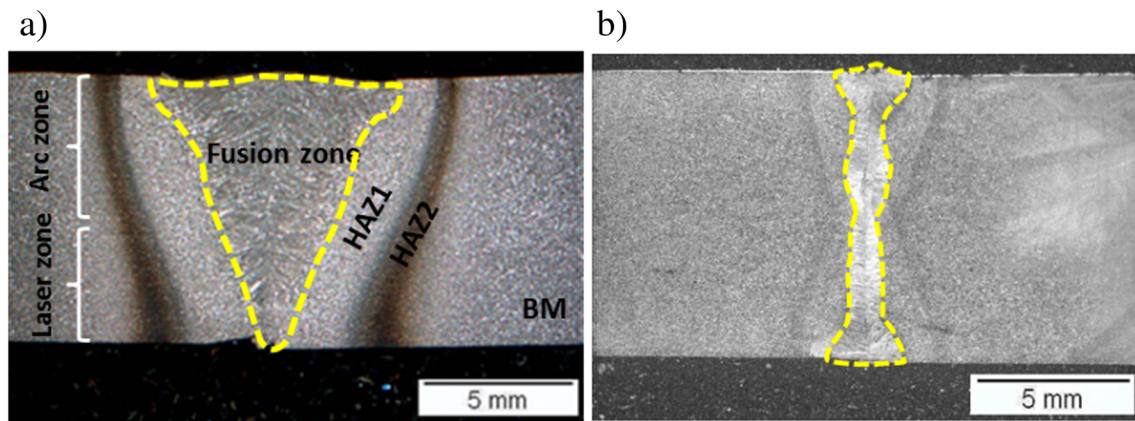


Fig. 4 Macrostructures of the joints **a** LHW and **b** ALW

and 25 mL H₂O for 10 min. Macrostructure of the weld cross section was taken using an Olympus stereo microscope. The microstructure of the welds etched with modified Fry's reagent (50 mL HCl, 25 mL HNO₃, 1 g CuCl₂, and 150 mL water) was studied using an opto-digital microscope. The chemistry of the fusion zone in as-welded condition was studied using inductively coupled plasma-optical emission spectroscopy (ICP-OES). The percentage of reverted austenite in the fusion zone microstructures after post-weld aging treatment was measured using image analysis software.

The microhardness measurements were carried out by a Vickers microhardness tester using a 200-g applied load on as-welded and post-weld aged specimens to characterize the different regions. The hardness tester was programmed in terms of number of indentations in the form of a fine grid across the transverse cross section of the sample. A grid of 22 mm (across the fusion zone at 0.2-mm intervals) × 10 mm (in plate thickness direction at an interval of 2 mm) was programmed. A total of 500 indentations per weld were made. The microhardness values were measured and plotted as a contour. Transverse weld tensile tests were carried out on specimens of rectangular cross section as per ASTM E8 in both as-welded and post-weld aged conditions. All the tests were conducted using the Instron 5985 universal testing machine of 250 kN capacity at a cross head speed of 2 mm/min at room temperature. In order to evaluate K_{Ic}

fracture toughness of the welds, compact tension (CT) specimens with straight notch were made as per ASTM E399, with the notch located at the center of the transverse section of the fusion zone. The fatigue pre-cracking and the crack open displacement (COD) test was conducted as per standards using the Dartec universal testing machine of 10 tonnes capacity. For pre-cracking, the input loading conditions were 0.3 to 3 kN till crack initiation. After crack initiation, the load was reduced by 0.05 kN and varied from 0.25 to 2.5 kN. The COD test was done at 0.5 kN/s.

3 Results and discussion

3.1 Macrostructure and microhardness

The cross-sectional macrographs of LHW and ALW joints are shown in Fig. 4. Macroetching of the transverse cross section revealed three distinct regions: (a) fusion zone, (b) light-etched HAZ/HAZ1, and (c) dark-etched HAZ (eyebrow zone)/HAZ2. The hybrid welds showed typical “wine-cup” shape, including the wider upper arc zone and the narrow lower laser zone. The ALW welds revealed narrow fusion zone and HAZ. The bead geometry measurements such as bead width, penetration depth, and the width of the HAZ are given in Table 3. LHW weld exhibited the wider arc fusion zone (AFZ) and narrow laser fusion zone (LFZ) as seen in Fig. 4. The width of HAZ varied along the fusion line from 2.5 to 4.4 mm, accompanied by variation in HAZ2 width from 0.8 to 1.8 mm. ALW weld exhibited a narrow fusion zone and minimum HAZ2 width of 0.3–0.4 mm. It can be inferred from the available literature that narrow HAZ2 eliminates issues with respect to the weld integrity and may not be of practical significance [6].

Microhardness contour plots of the transverse cross section in as-welded and post-weld aged conditions corresponding to LHW and ALW joints are shown in Fig. 5. The variation in hardness throughout the welds confirmed the presence of different zones which has formed due to variation in peak

Table 3 Bead geometry measurements of the joints

Bead geometry measurements		LHW	ALW
Fusion area (mm ²)		34.5	14.6
Bead width (mm)	Arc zone	8.9	2.6
	Laser zone	0.9	
Penetration depth (mm)	Arc zone	8.2	6.5 mm per pass
	Laser zone	1.8	
*Total HAZ width (mm)		2.5–4.1–4.4	1.6–1.6–1.1
*HAZ2 width (mm)		0.8–1.3–1.8	0.4–0.3

*Values were reported at 1, 5, and 9 mm in transverse cross section of the weld from top surface

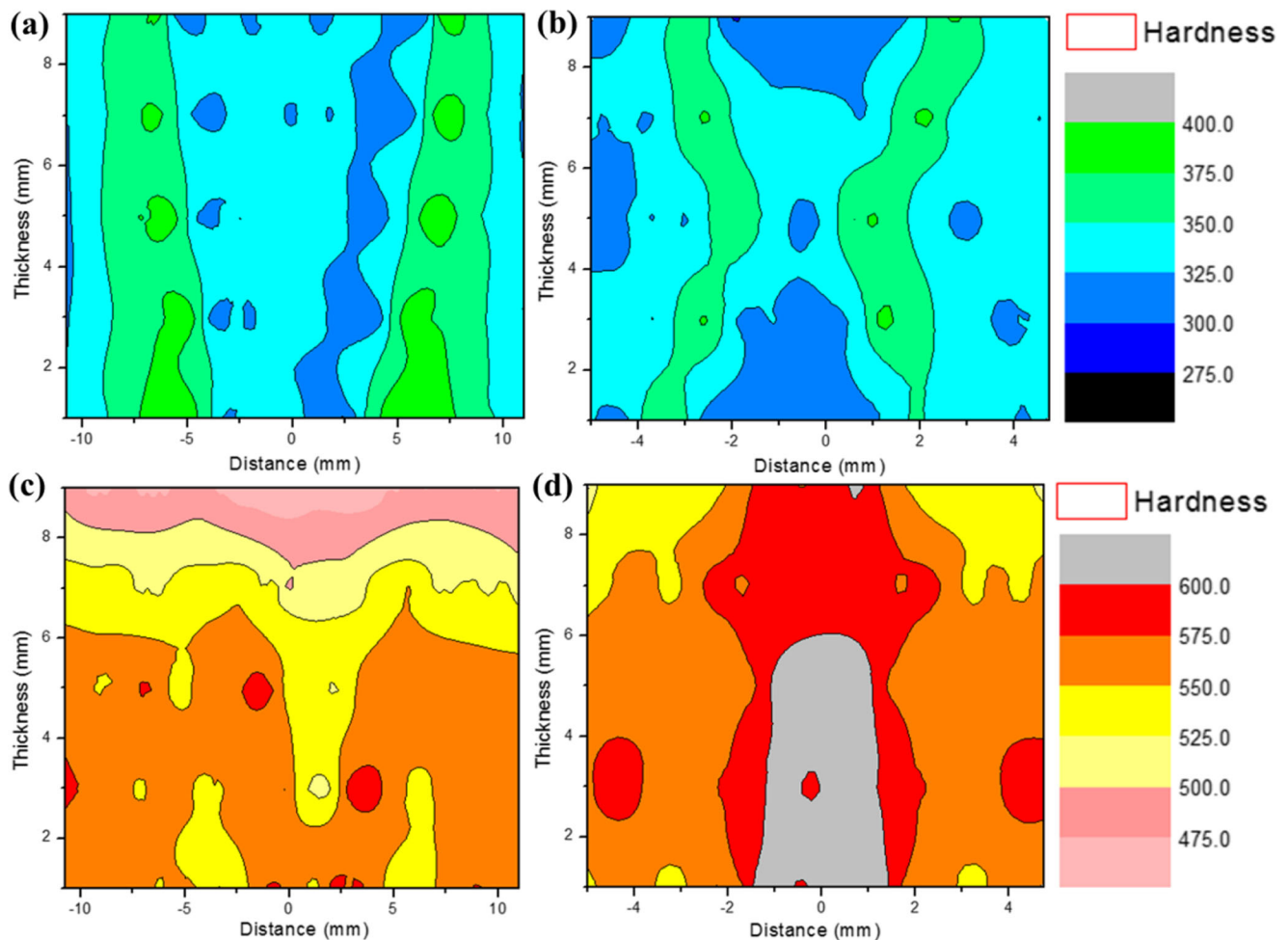


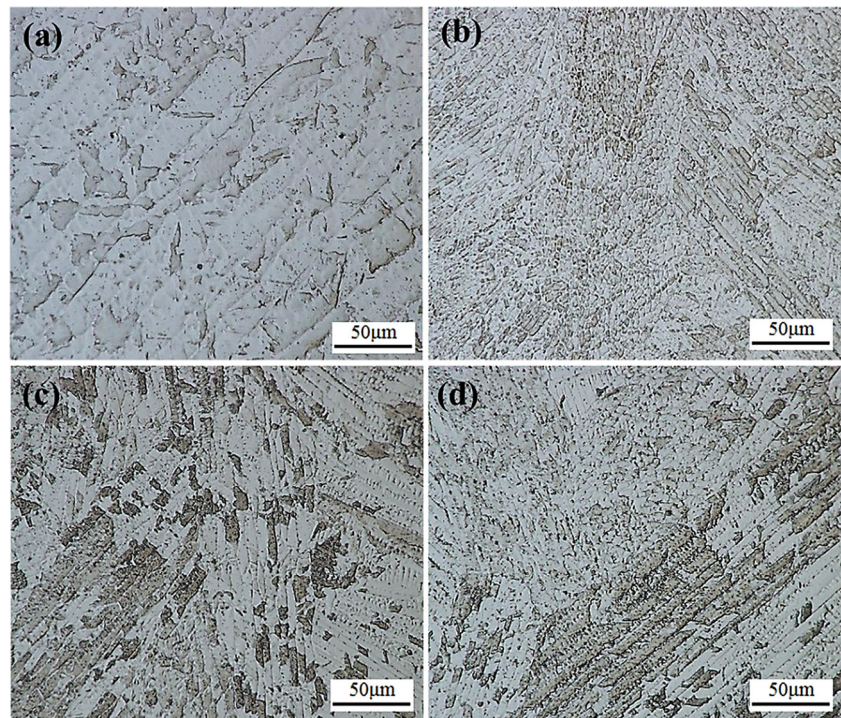
Fig. 5 Hardness contour plots of a transverse cross section of weld in **a** LHW as-welded, **b** ALW as-welded, **c** LHW post-weld aged, and **d** ALW post-weld aged

temperature experienced at different regions during welding. The as-received base metal showed hardness of 350 HV. The hardness of arc and laser fusion zone of LHW and fusion zone of ALW weld was found to be similar to that of the base metal hardness and was in the range 300–350 HV. The grain size or the microsegregation in the dendritic boundaries was not found to affect the hardness values in the as-welded condition. During welding, the HAZ1 experiences temperature in the austenite region of the Fe-Ni phase diagram and transforms back to soft lath martensitic structure similar to that of the base metal. The hardness of HAZ1 was in the range 325–350 HV. The HAZ2 experiences temperature in the aging temperature regime because of which it develops precipitates during welding, even at a high welding speed of 1 m/min. The maximum hardness was exhibited by HAZ2 (375–400 HV).

After post-weld aging treatment, the base metal hardness increased to 575 HV due to the formation of hardening precipitates. The fusion zone of LHW weld exhibited a lower hardness of 500–550 HV. On the other hand, the hardness of the ALW fusion zone was the highest in the range 575–600 HV with the fusion zone of pass 2, even

exceeding 600 HV (600–620 HV). It is expected that the high hardness is due to the finer grain size of ALW fusion zone which is characteristic of a laser weld [12]. In addition to this, the ALW fusion zone would be rich in precipitate forming elements since it involves melting and solidification of base metal. This might have resulted in a high number density of precipitates within the zone, when compared with LHW weld, which was welded using filler wire with reduced solute contents. This understanding is explained further in the discussion on fusion zone microstructure. The HAZ1 of LHW weld exhibited hardness similar to the base metal with hardness value 550–575 HV, and hardness of HAZ2 was in the range 525–550 HV. The HAZ1 and HAZ2 of ALW welds exhibited similar hardness as that of the base metal and were in the range 550–575 HV. Welding thick plates in a single pass at a comparatively low heat input using LHW and ALW processes has helped in maintaining the hardness of the HAZ2 unlike arc welding processes where the multiple passes of welding deteriorate the properties of the HAZ2 due to coarsening of precipitates [4, 25].

Fig. 6 Fusion zone optical micrographs in as-welded condition showing solidification characteristics of **a** AFZ and **b** LFZ of LHW weld and **c** pass 1 and **d** pass 2 of ALW weld at $\times 1000$ magnification



3.2 Microstructure of the fusion zone

The optical micrographs of the arc and the laser fusion zones (AFZ and LFZ) of the hybrid weld in as-welded condition are shown in Fig. 6 a and b respectively. The optical micrographs

of the fusion zone corresponding to passes 1 and 2 of ALW weld in the as-welded condition are shown in Fig. 6 c and d respectively.

The microstructure of the FZ is governed by composition and cooling rate [26]. The arc fusion zone of the LHW weld

Fig. 7 Fusion zone optical micrographs in post-weld aged condition showing white pools of RA at intercellular or interdendritic regions in **a** AFZ and **b** LFZ of LHW weld and **c** pass 1 and **d** pass 2 of ALW weld at $\times 2220$ magnification

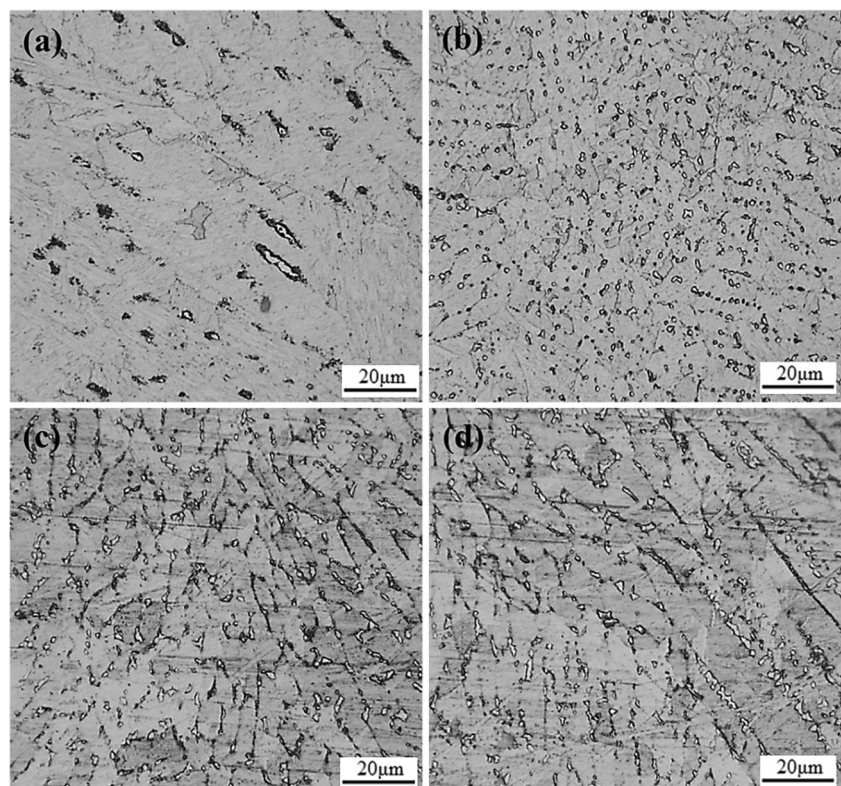


Table 4 Ni, Mo, and Ti contents in the as-welded fusion zone and base metal (wt%) by ICP-OES

Process	Location	Ni	Mo	Ti
Base metal		20.43	5.3	0.44
LHW	AFZ	16.88	4.07	0.23
	LFZ	17.15	4.18	0.21
ALW	Pass 1	19.42	4.94	0.43
	Pass 2	19.24	4.86	0.48

exhibited solidification structure mainly of columnar dendrites similar to that of a typical arc weld. This behavior is because of the low power density of the MIG arc that had resulted in low-temperature gradient and growth rate. On the other hand, the laser fusion zone exhibited solidification characteristics similar to that of a typical laser weld since this region experiences the effect of the high power density of the laser keyhole. Due to the high cooling rates in LFZ, it showed a much finer structure than the AFZ. A high cooling rate typically is experienced by the melt pool immediately after autogenous laser welding. Solidification takes place usually in few tens of milliseconds because of which the ALW fusion zones exhibited finer columnar/columnar dendritic structures similar to that of LFZ in LHW welds [27, 28].

The optical micrographs of the arc and the laser fusion zones (AFZ and LFZ) of the hybrid weld in aged condition are shown in Fig. 7 a and b respectively. The optical micrographs of the fusion zone corresponding to passes 1 and 2 of ALW weld in the aged condition are shown in Fig. 7 c and d respectively. Aging in maraging steels involves two important reactions such as the formation of intermetallic precipitates, which contribute to the strength of the steel [2] and austenite reversion in the solute-rich regions which deteriorate the mechanical performance of the steel [5, 6]. The fusion zones of the welds show clear interdendritic phases (white pools) which are the reverted austenite. The size and distribution of the RA

Table 5 EDS elemental analysis of the fusion zones corresponding to LHW and ALW welds given in wt%. Representations used are DB (dendritic boundary) and M (matrix)

Process	Zone	Region	Ni	Co	Mo	Ti	Al	Fe
LHW	AFZ	DB	17.34	8.23	5.145	0.66	0.14	68.48
		M	17.18	8.37	3.56	0.42	0.11	70.36
	LFZ	DB	18.28	8.79	5.525	0.895	0.16	66.24
		M	17.35	8.39	3.47	0.25	0.11	70.33
ALW	Pass 1	DB	17.72	7.3	6.97	0.82	0.095	67.07
		M	17.82	7.65	5.2	0.13	0.12	68.98
	Pass 2	DB	18.34	6.47	5.78	0.21	0.19	69
		M	17.98	6.29	5.09	0.16	0.05	70.42

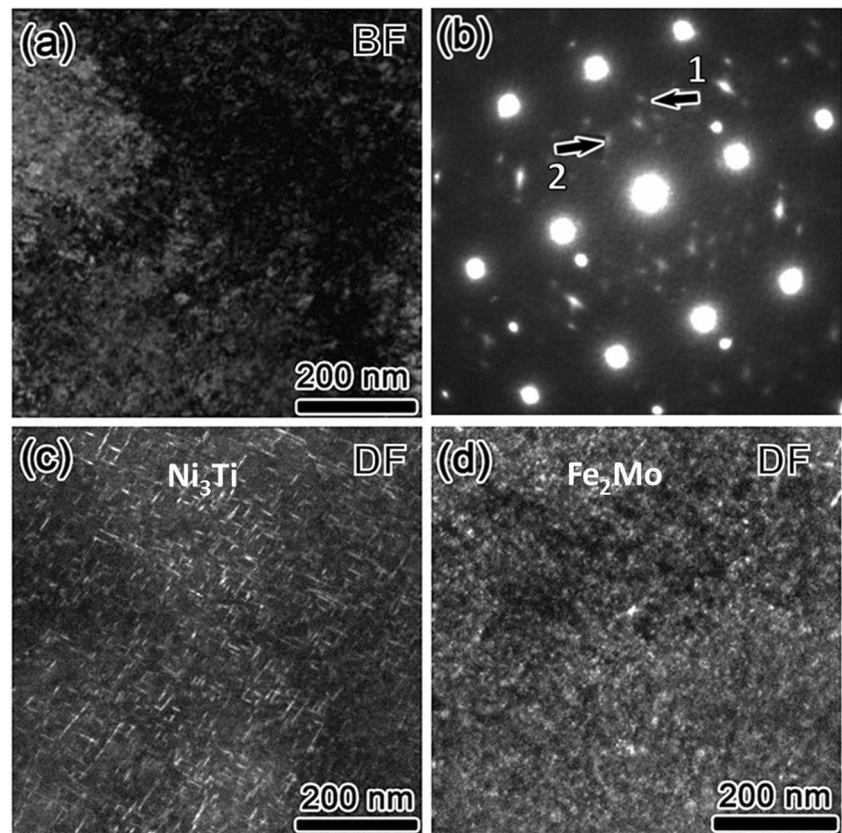
were found to be dependent on the solidification structure. In the case of LHW weld, LFZ showed finer RA compared with AFZ.

3.3 Fusion zone: chemistry in as-welded condition and % RA after post-weld aging

The chemistry of fusion zone in as-welded condition determines the number density of precipitates as well as the volume fraction of reverted austenite in aged condition. In a laser hybrid weld, the resulting fusion zone composition can be equivalent to filler wire composition in the arc zone and equivalent to base metal composition in the laser zone. For the experiment conditions considered such as Y-groove edge preparation and 0.2-mm gap between plates and filler wire positioned at the root face, the base metal dilution may not be homogeneous throughout the thickness of the weld [24]. The wt% of the solutes Ni, Mo, and Ti are important in determining the austenite and precipitate content within the fusion zone. Hence, the analysis of the fusion zone chemistry in as-welded condition individually in the arc and laser fusion zones of LHW weld and the two passes of ALW welds was done using ICP-OES with respect to these three elements. The results of the analysis are compared with the as-received base metal composition as given in Table 4. A clear variation in the wt% of solutes was observed between the fusion zones of LHW and ALW welds. The LHW fusion zone had less amount of Ni, Mo, and Ti both in the arc and in the laser fusion zones when compared with the ALW fusion zone. Hence, the extent of microsegregation of the solutes is expected to be minimum in LHW weld, and very less or negligible RA could be expected in the fusion zone after aging. The fusion zone chemistry of ALW weld, which was made without filler wire, was near to the base metal composition. Considering the very low heat input of the ALW process, less microsegregation of solutes occurs during weld solidification which could possibly lead to lower volume fraction of RA after aging.

EDS elemental mapping of the fusion zone did not reveal clear segregation of the solute elements at the dendritic boundaries due to the reduced extent of solute segregation during LHW and ALW processes as compared with the three-pass MIG welding of 10-mm-thick maraging steel plates [25]. Hence, EDS point scans were performed at the interdendritic boundaries (DB) and compared with the matrix (M) to understand the extent of microsegregation. Point scans revealed segregation of solute elements at the dendritic boundaries. Analysis of the segregation pattern of elements in the areas shown in Table 5 reveals that there was no pronounced segregation of Ni and Co in some cases, but Mo and Ti was found to strongly segregate at the dendritic boundaries. The tendency of these four elements to segregate is found to be in agreement with their partition coefficient calculated from their binary phase diagram with Fe [8].

Fig. 8 Maraging steel aged base metal: **a** BF micrograph; **b** $[110]_M$ SAD pattern; **c** DF micrograph taken from the Ni_3Ti spot labeled 1 in **b**; and **d** DF micrograph taken from Fe_2Mo spot labeled 2 in **b**



The quantification of RA pools present in each zone after aging was done using image analysis software. For the image analysis, at least 15 images were taken from different regions within the fusion zone of the welds. The LHW fusion zone showed a minimum amount of RA with an average of 2.5% and 2.6% in AFZ and LFZ respectively. The ALW weld fusion zone exhibited a comparatively high amount of RA with an average of 5.6% and 5.9% in passes 1 and 2 respectively. Considering a similar instance in a GMAW weld where the weld metal composition was similar to the base metal, 14.5% RA was reported [6]. The high RA content in GMAW weld, when compared with that in the ALW weld, is due to the high heat input of the GMAW process, which might have resulted in a high degree of solute segregation. On the other hand, the addition of filler wire with reduced solute content for LHW process has helped in minimizing the amount of RA in the fusion zone, even less when compared with the fusion zone created by high power density autogenous laser welding process. This clearly explains the metallurgical advantages of using filler wire by laser hybrid welding process when compared with autogenous laser welding for welding thick sections of maraging steels.

Transmission electron microscopic studies were done on the aged samples extracted from the base metal. The fully dislocated martensite favors homogeneous distribution of the precipitates throughout the matrix. The existence of high

density of mobile dislocations results in good ductility. Ni_3Mo and Ni_3Ti are the first phases to be formed during the early stages of aging. Being a metastable phase, Ni_3Mo dissolves in the matrix as the aging progresses, causing two subsequent effects: (1) formation of stable Fe-Mo precipitates and (2) enrichment of Ni, encouraging austenite formation. The Ni_3Ti precipitates are responsible for the initial hardening and are stable throughout the precipitation process. The Fe_2Mo precipitates are responsible for the peak strength and maintenance of high strength for longer duration. Figure 8 a shows the BF image of the thermally aged base metal specimen. It consists of martensite matrix with high dislocation density. A uniform distribution of very fine intermetallic precipitates could also be seen, which appears to have nucleated on the martensite lath boundaries and the dislocations. The SAD pattern in Fig. 8 b obtained from matrix using the $[110]$ zone axis showed superlattice reflections corresponding to these precipitates. These SAD patterns have been indexed and the precipitates identified as Ni_3Ti and Fe_2Mo by Vasudevan et al. [2] and Viswanathan et al. [29]. Figure 8 c shows the dark-field image taken from the Ni_3Ti spot labeled 1 in Fig. 8 b. It revealed thin, needle-like precipitates of 5 nm wide and 20–40 nm long. These fine needles were found to be evenly distributed and in different orientations with respect to the matrix. There are twelve possible variants of Ni_3Ti relative to martensite [30]. Figure 8 d shows the dark-field image

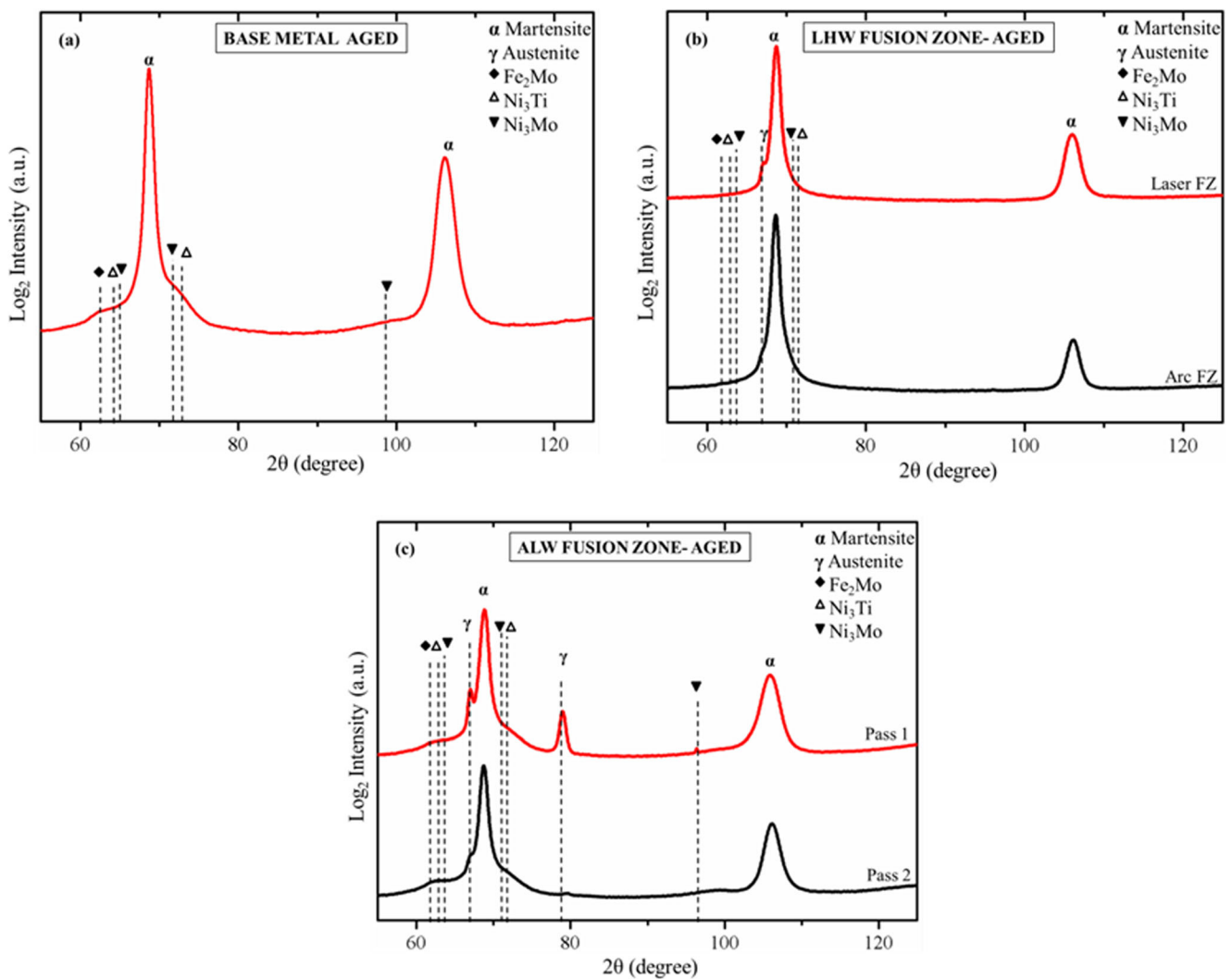


Fig. 9 Micro-XRD patterns obtained from **a** base metal, **b** LHW weld fusion zone, and **c** ALW weld fusion zone

taken from the Fe_2Mo spot labeled 2 in Fig. 8 b. Numerous spherical particles with an average size of 5 nm could be seen uniformly distributed in the matrix.

The micro-XRD studies were done in the aged base metal and the fusion zones. Micro-XRD pattern from aged base metal revealed peaks corresponding to Fe-Ni martensite and additional peaks corresponding to precipitates. The precipitates were identified to be Ni_3Ti , Fe_2Mo , and Ni_3Mo . The intensities of the precipitate peaks were less due to the low volume fraction, and there was an overlap of the peaks due to the close similarities in structure and d-spacing [2]. Micro-XRD patterns of the AFZs and LFZs corresponding to the hybrid welds and pass 1 and pass 2 of the ALW welds revealed peaks corresponding to austenite in addition to the peaks corresponding to martensite and the precipitates. Quantification of precipitate fraction in maraging steels is also quite difficult because of the small precipitate size and its low volume fraction. By comparing the intensities of the precipitate peaks of the fusion zones corresponding to both the

processes from Fig. 9, it could be concluded qualitatively that the volume fraction of precipitates in ALW fusion zone is high when compared with that in LHW fusion zone. This is because of the fact that the ALW fusion zone was formed by melting and solidification of the base metal, which is rich in solutes.

3.4 Tensile properties and fracture toughness evaluation

The tensile properties such as 0.2% yield strength (YS), ultimate tensile strength (UTS), and percentage of elongation were evaluated for the base metal and transverse cross sections of the joints in aged conditions. The sample dimensions for tensile and K_{Ic} fracture toughness measurements and its location on the welded plate are shown in Fig. 10.

The results of the tests are given in Table 6. The stress-strain curves obtained from the tensile testing of base metal and LHW and ALW welds are shown in Fig. 11. The aged base metal

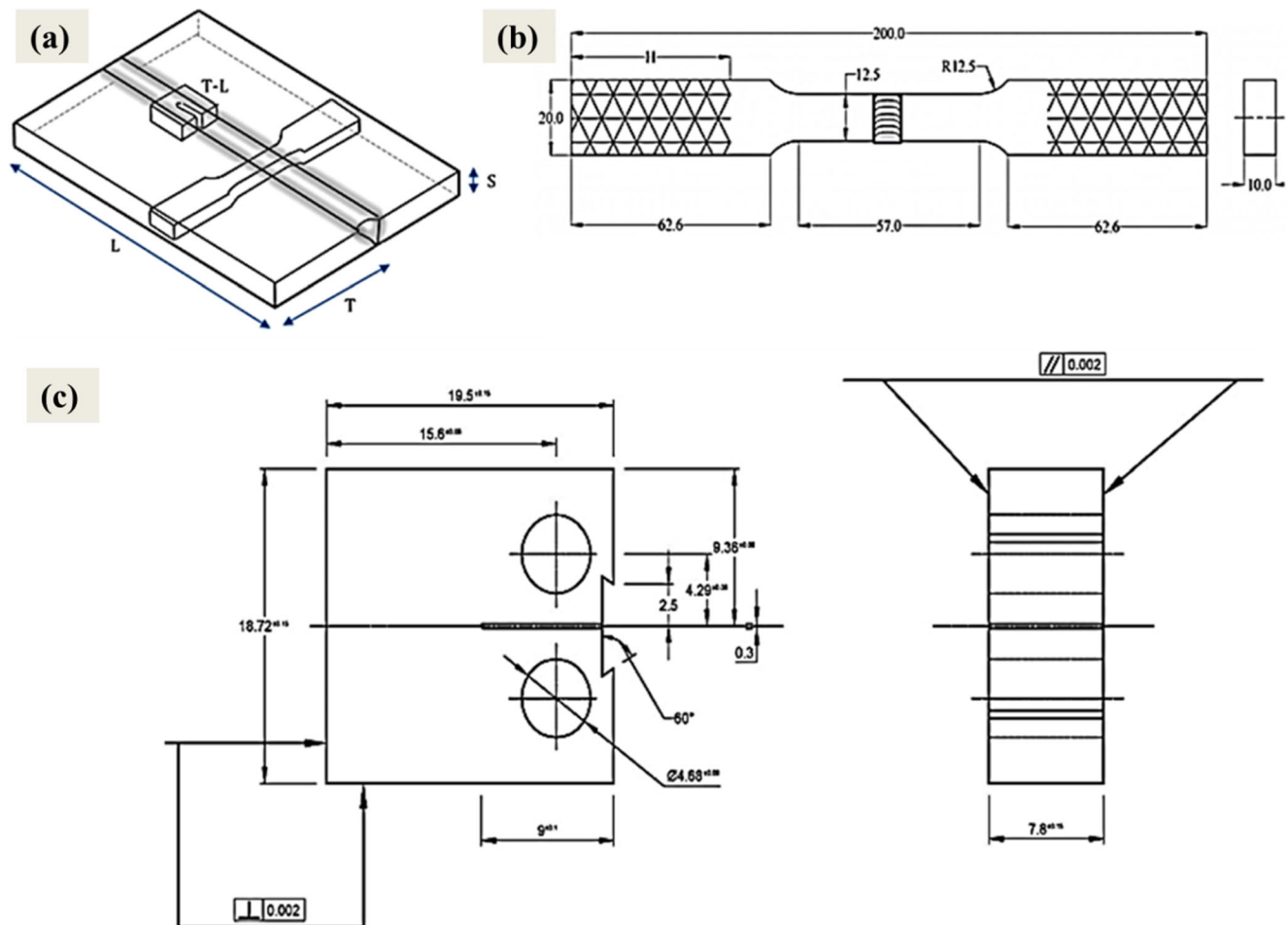


Fig. 10 **a** Location of test specimens, **b** transverse tensile test specimen as per ASTM E8, and **c** K_{Ic} straight notch specimen as per ASTM E399 (all dimensions in mm)

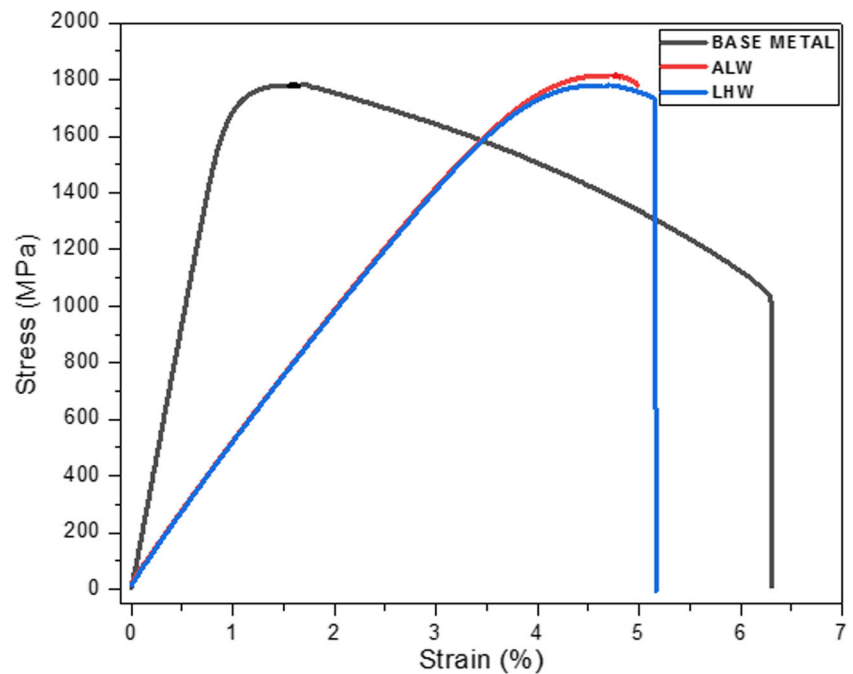
yielded YS and UTS of 1655 MPa and 1778 MPa respectively with 10% elongation. During transverse weld tensile testing of the LHW and ALW welded samples in aged condition, failure occurred in the fusion zone with a considerable reduction in ductility. The fracture surfaces of the tensile tested base metal, AFZ, and LFZ of laser hybrid weld and ALW weld are shown in Fig. 12 a, b, c, and d respectively. It can be seen that the fracture surfaces were composed of equiaxed dimples of different sizes. The size of the dimples in base metal was larger, indicating good plasticity. The LHW welds in aged condition exhibited YS and UTS of 1659 MPa and 1783 MPa respectively with 3% elongation. The ALW welds in aged condition exhibited YS and UTS

of 1727 MPa and 1817 MPa respectively with 3.8% elongation. The fractured surface of the AFZ of LHW weld showed finer dimples compared with that of the base metal. The LFZ of LHW weld and the ALW fractured surface exhibited very fine dimples than the AFZ. Thus, the sizes of the dimples were associated with the grain size. The ALW joints exhibited the maximum strength due to the fine grain structure of laser welds. In addition to this, the ALW fusion zone would have high number density of precipitates as it was formed by melting and solidification of the base metal which has high solutes content. This observation goes in hand with the high value of microhardness exhibited by the ALW fusion zone. It has to be noted that even though the ALW

Table 6 Mechanical properties of M250 maraging steel plate and welded specimens

Sample	Transverse weld tensile properties				Fusion zone		
	0.2% YS (MPa)	UTS (MPa)	% El	Fracture location	Hardness (HV _{0.2})	K_{Ic} (MPa√m)	Absorbed energy (J/m ³)
Base metal aged	1655	1778	10	-	575	110	89
LHW aged	1659	1783	3	Fusion zone	500–550	77.5	59
ALW aged	1727	1817	3.8	Fusion zone	575–620	49.5	56

Fig. 11 Stress-strain curves obtained from tensile testing of base and weld metals



weld showed greater than 5% RA in the fusion zone, it was not found to affect the transverse weld tensile strength and has yielded high strength values compared with the LHW weld. It is known that the area underneath the stress-strain curve would be equal to the toughness of the material which represents the ability to absorb mechanical energy of material in its unit volume up to failure [31–33]. It can be seen from Table 6 that the maximum energy absorbed (i.e.) toughness of 89 J/m^3 was obtained in base metal while the laser hybrid weld and autogenous laser weld showed toughness of 59 J/m^3 and 56 J/m^3 respectively.

The K_{Ic} fracture toughness of weld fusion zones in aged condition was evaluated using compact tension (CT) specimen with a straight notch, with notch and fatigue cracked at the center of the fusion zone and longitudinal to the weld as shown in Fig. 10 a. The K_{Ic} value of the base metal in the aged condition was $110 \text{ MPa}\sqrt{\text{m}}$. The K_{Ic} values of the fusion zones of the LHW and ALW welds in aged condition were 77.5 and $49.5 \text{ MPa}\sqrt{\text{m}}$ respectively. Even though the presence of reverted austenite did not affect the strength of the welds, it was found to greatly affect the fracture toughness of the welds. Similar behavior has been

Fig. 12 SEM micrographs of the fractured surfaces of tensile tested samples in the aged condition: a base metal; b, c AFZ and LFZ of LHW weld; d ALW weld

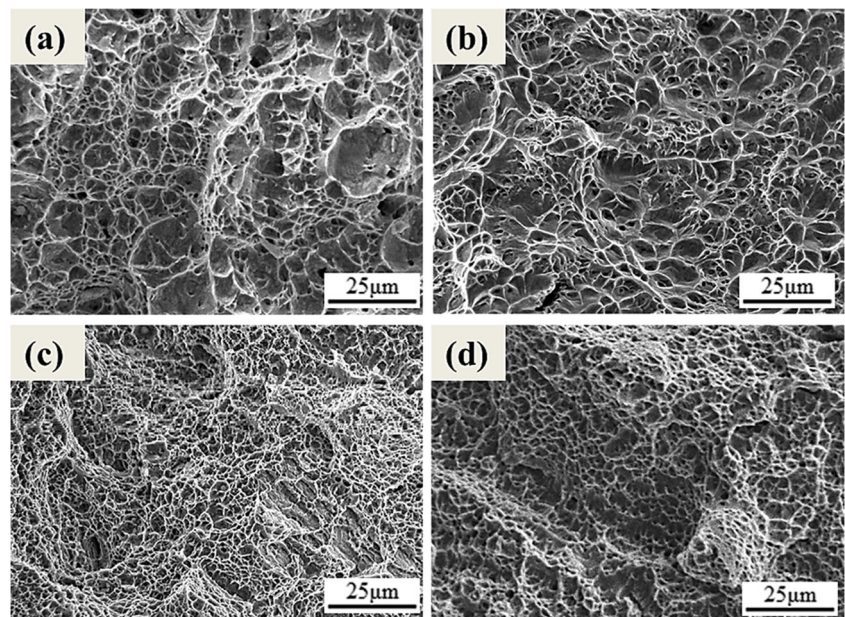
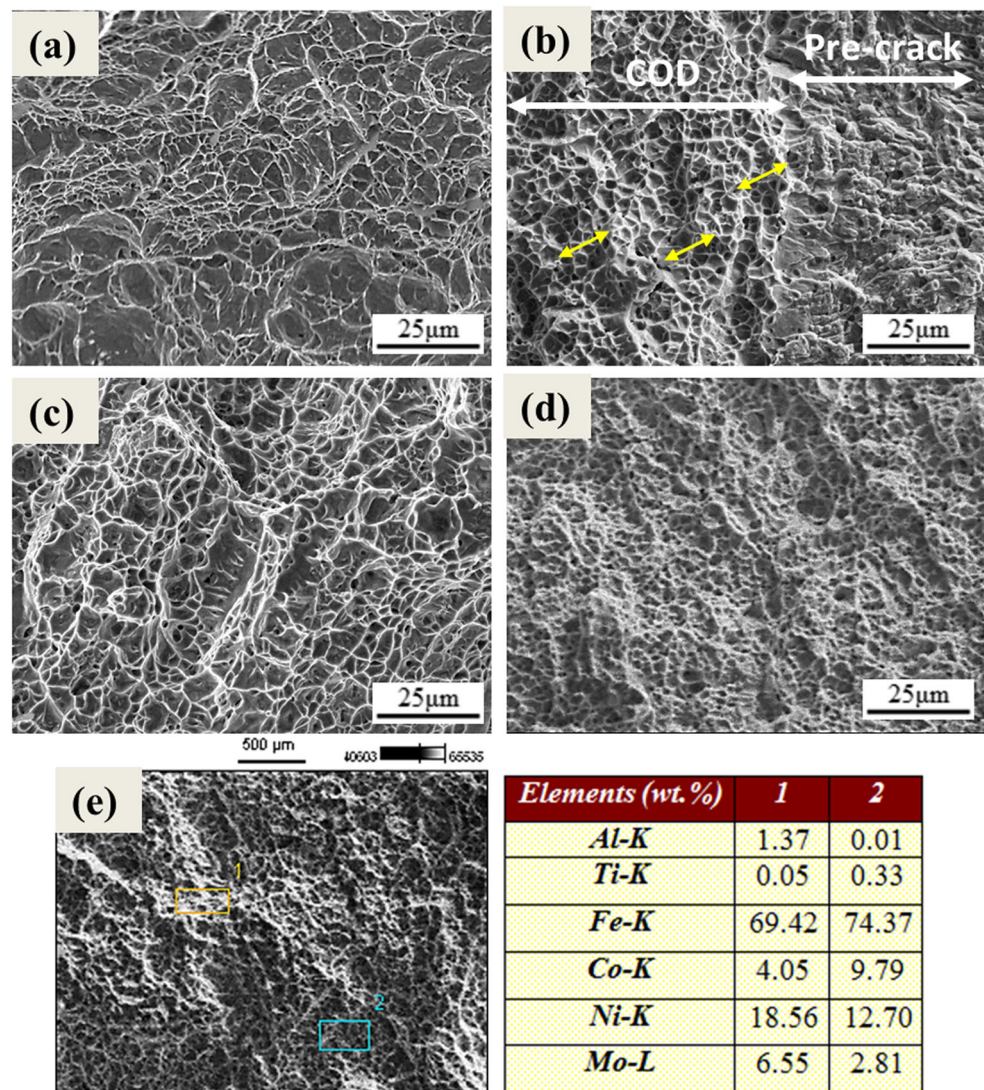


Fig. 13 SEM micrographs of fracture toughness tested samples in aged condition showing COD fractured surface of **a** base metal, **b** fatigue pre-crack and COD fracture surface in AFZ and **c** LFZ of LHW weld and **d** ALW weld, and **e** EDS elemental composition analysis on COD fractured surface of ALW weld



reported during maraging steel welding using all the fusion processes [4–6]. Only in case of solid-state welding processes such as friction stir welding of 5.5-mm-thick M250 maraging steel using W-Mo tool resulted in a weld nugget in which RA was absent, resulting in superior impact properties [34].

The fracture surface after COD testing of base metal revealed different sizes of equiaxed dimples formed due to microvoid coalescence. The fracture surface of the weld exhibited finer equiaxed dimples. One distinct feature was the presence of highly reflective features (marked with arrows in Fig. 13 b) at regular intervals, which correspond to the fracture path associated with dendritic boundaries where soft RA pools are distributed. EDS analysis of the two regions shown in Fig. 13 e revealed significant variation in the amount of Ni, Mo, and Ti which supports the above discussion.

The ALW welds yielded higher strength values than LHW and base metal due to the fine grain size. On the other hand,

the ALW weld fusion zone exhibited a very low fracture toughness value, which is due to the presence of a high volume fraction of RA. The size of the RA pools was less in the ALW fusion zone and LFZ of LHW welds when compared with that in the AFZ. It is known that the RA pools are formed in the interdendritic/intercellular boundaries and the welds containing austenite fail by linking a series of voids which form only in the austenite pool. Because of the finer structure in the ALW fusion zone, the intercellular spacing or the mean free path of the cells is less [6]. Hence, the distance between the adjacent RA pools is less in the ALW fusion zone than in the LHW fusion zone, which is the primary reason for lower toughness of fusion zone of ALW than that in the case of LHW. The results established that laser hybrid welding resulted in welds with less amount of austenite compared with autogenous laser welding and other conventional fusion welding processes [4–6] resulting in improved fracture toughness of the welds.

4 Conclusions

1. The chemistry of the LHW joint showed less Ni, Mo, and Ti when compared with the base metal due to the usage of filler wire with reduced solute content. The composition of the ALW fusion zone matched with that of the base metal since it involved melting and solidification of only the base metal.
2. The volume fraction of RA formed after aging was dependent on the as-welded fusion zone chemistry. The LHW joint had 2.5% and 2.6% RA in AFZ and LFZ respectively, whereas the fusion zone of ALW joint showed greater than 5% RA after aging.
3. While the joint efficiencies were as good as the base metal, K_{Ic} fracture toughness values reduced considerably. The ALW fusion zone showed a very low K_{Ic} fracture toughness value of 49.44 MPa \sqrt{m} . The LHW fusion zone exhibited comparatively better K_{Ic} fracture toughness of 77.4 MPa \sqrt{m} .
4. The fine structure and high volume fraction of precipitates contributed to high strength in ALW welds. On the other hand, fine structure means less intercellular spacing (the spacing between RA pools). Hence, the fusion zone of ALW weld failed easily by linking a series of voids which formed in the soft austenite pool.
5. LHW resulted in welds with comparatively lesser volume fraction of austenite as compared with ALW. By optimization of process parameters, it was possible to produce welds with substantially low volume fraction of reverted austenite and hence improved fracture toughness.

Acknowledgments We are thankful to Mr. E. Anbu Rasu, ARCI, for his assistance in carrying out the welding experiments. We thank DRDL for their support with the material as well as for mechanical testing. Also, we are thankful to Dr. Joydip Joardar, Scientist, ARCI, for his help in performing Micro-XRD scans. We would also like to thank all those who have either directly or indirectly extended their help in carrying out the studies.

References

1. Sundaresan S, Manirajan M, Nageswara Rao B (2010) On the fracture toughness evaluation in weldments of a maraging steel rocket motor case. *Mater Des* 31:4921–4926
2. Vasudeven VK, Kim SJ, Marvin Wayman C (1990) Precipitation reactions and strengthening behavior in 18 Wt Pct nickel maraging steels. *Metall Trans A* 21A:2655–2668
3. Decker RF (1979) Notes on the development of maraging steels, Source book on maraging steels, Pub by ASM, Metals Part, Ohio
4. Tariq F, Baloch RA, Ahmed B, Naz N (2010) Investigation into microstructures of maraging steel 250 weldments and effect of post-weld heat treatments. *JMEPEG* 19, ASM International. pp 264–273
5. Shamantha CR, Narayanan R, Iyer KJL, Radhakrishnan VM, Seshadri SK, Sundararajan S, Sundaresan S (2000) Tensile properties and fracture toughness of 18Ni (250 grade) maraging steel weldments. *Sci Technol Weld Join* 5(5):329–337
6. Kenyon N (1968) Effect of austenite on the toughness of maraging steel welds. *Welding Research Supplement* pp 193–198s
7. Bagchi A, Gope DK, Chattopadhyaya S (2019) A critical review on susceptibility of stress corrosion cracking in maraging steel weldments. *Mater Today Proc.* <https://doi.org/10.1016/j.matpr.2019.09.117>
8. Shamantha CR, Narayanan R, Iyer KJL, Radhakrishnan VM, Seshadri SK, Sundararajan S, Sundaresan S (2000) Microstructural changes during welding and subsequent heat treatment of 18Ni (250-grade) maraging steel. *Mater Sci Eng A287*:43–51
9. An J, Meng F, Lv X, Liu H, Gao X, Wang Y, Lu Y (2012) Improvement of mechanical properties of stainless maraging steel laser weldments by post-weld ageing treatments. *Mater Des* 40: 276–284
10. Fanton L, Abdalla AJ, Fernandes de Lima MS (2014) Heat treatment and Yb-fiber laser welding of a maraging steel. *Weld J* 93: 362-s–3368s
11. Katz R, Zak A, Shirizly A et al (2018) Method for producing porosity-free joints in laser beam welding of maraging steel 250. *Int J Adv Manuf Technol* 94:2763
12. Van Rooyen C, Burger HP, Kazadi P, & Kriek C (2006) Comparison of CO₂ and Nd:YAG laser welding of grade 250 maraging steel. *IIW Doc. II-A-173-06*
13. Venkateswara Rao V, Madhusudhan Reddy G, Sitarama AV (2010) Influence of postweld heat treatment on the microstructure and mechanical properties of maraging steel electron beam weldments. *Steel Grips* 8:434–440
14. Murthy CVS, Gopala Krishna A, Madhusudhan Reddy G (2019) Dissimilar welding of maraging steel (250) and 13-8 Mo stainless steel by GTCAW, LBW and EBW processes. *Trans Indian Inst Met* 72:2433
15. Murthy CVS, Gopala Krishna A, Madhusudhan Reddy G (2019) Microstructure and mechanical properties of similar and dissimilar metal gas tungsten constricted arc welds: Maraging steel to 13-8 Mo stainless steel. *Def Technol* 15(1):111–121
16. Gupta R, Reddy R, Mukherjeekey MK (2012) Key-hole plasma arc welding of 8 mm thick maraging steel- a comparison with multi-pass GTAW. *Weld World* 2012(56):69–75
17. Ribic B, Palmer TA, DebRoy T (2009) Problems and issues in laser-arc hybrid welding. *Int Mater Rev* 54(4):223–244
18. Padmanabham G, Shanmugarajan B, Phani Prabhakar KV (2012) Laser-MIG hybrid welding of thick plates of mild steel in single pass. *Indian Weld J* 45(2):29–39
19. Mazar Atabaki M, Ma J, Liu W, Kovacevic R (2015) Pore formation and its mitigation during hybrid laser/arc welding of advanced high strength steel. *Mater Des* 67:509–521
20. Bunaziv I, Akselsen OM, Frostevarg J et al (2019) Application of laser-arc hybrid welding of steel for low-temperature service. *Int J Adv Manuf Technol* 102:2601
21. Li C, Liu L (2013) Investigation on weldability of magnesium alloy thin sheet T-joints: arc welding, laser welding, and laser-arc hybrid welding. *Int J Adv Manuf Technol* 65:27–34
22. Jiang Z, Hua X, Huang L et al (2018) Double-sided hybrid laser-MIG welding plus MIG welding of 30-mm-thick aluminium alloy. *Int J Adv Manuf Technol* 97:903–913
23. Li R, Zhang F, Sun T et al (2019) Investigation of strengthening mechanism of commercially pure titanium joints fabricated by autogenously laser beam welding and laser-MIG hybrid welding processes. *Int J Adv Manuf Technol* 101:377–389
24. Subashini L, Phani Prabhakar KV, Gundakaram RC, Ghosh S, Padmanabham G (2016) Single pass laser-arc hybrid welding of maraging steel thick sections. *Mater Manuf Process* 31(16):2186–2198
25. Subashini L, Phani Prabhakar KV, Padmanabham G. (2014) Laser-MIG hybrid welding of maraging steel; in Proceedings of the

- Conference of Metallurgists COM- 2014, Published by the Canadian Institute of Mining, Metallurgy and Petroleum, ISBN: 978-1-926872-24-7
26. Kou S (2003) *Welding metallurgy*. A Wiley-interscience publication, Hoboken, p 166
 27. Fotovvati B, Wayne SF, Lewis G, Asadi E (2018) A review on melt-pool characteristics in laser welding of metals. *Adv Mater Sci Eng*. <https://doi.org/10.1155/2018/4920718>
 28. Obidigbo C, Tatman EP, Gockel J (2019) Processing parameter and transient effects on melt pool geometry in additive manufacturing of Invar 36. *Int J Adv Manuf Technol* 104(5–8):3139–3146
 29. Viswanathan UK, Dey GK, Asundi MK (1993) Precipitation hardening in 350 grade maraging steel. *Metall Trans A* 24:2429
 30. Moshka O, Pinkas M, Brosh ME, Ezersky V, Meshi L (2015) Addressing the issue of precipitates in maraging steels – unambiguous answer. *Mater Sci Eng A* 638:232–239
 31. Khorrami MS, Mostafaei MA, Pouraliakbar H, Kokabi AH (2014) Study on microstructure and mechanical characteristics of low-carbon steel and ferritic stainless steel joints. *Mater Sci Eng A* 608:35–45
 32. Jandaghia MR, Pouraliakbar H (2017) Study on the effect of post-annealing on the microstructural evolutions and mechanical properties of rolled CGPed aluminum-manganese-silicon alloy. *Mater Sci Eng A* 679:493–503
 33. Pouraliakbar H, Jandaghi MR (2018) Mechanistic insight into the role of severe plastic deformation and post-deformation annealing in fracture behavior of Al-Mn-Si alloy. *Mech Mater* 122:145–158
 34. Suresh Meshram D, Madhusudhan Reddy G, Pandey S (2013) Friction stir welding of maraging steel (Grade-250). *Mater Des* 49:58–64

Publisher's note Springer Nature remains neutral with regard to jurisdictional claims in published maps and institutional affiliations.